nature physics

SUPPLEMENTARY INFORMATION

https://doi.org/10.1038/s41567-020-0949-y

In the format provided by the authors and unedited.

Realization of an anomalous Floquet topological system with ultracold atoms

Karen Wintersperger[1,2], Christoph Braun[1,2,3], F. Nur Ünal[4,5], André Eckardt[4,6], Marco Di Liberto[7], Nathan Goldman[7], Immanuel Bloch[1,2,3] and Monika Aidelsburger[1,2] ✉

[1]Fakultät für Physik, Ludwig-Maximilians-Universität München, Munich, Germany. [2]Munich Center for Quantum Science and Technology (MCQST), Munich, Germany. [3]Max-Planck-Institut für Quantenoptik, Garching, Germany. [4]Max-Planck-Institut für Physik komplexer Systeme, Dresden, Germany. [5]T.C.M. Group, Cavendish Laboratory, Cambridge, UK. [6]Institut für Theoretische Physik, Technische Universität Berlin, Berlin, Germany. [7]Center for Nonlinear Phenomena and Complex Systems, Université Libre de Bruxelles, Brussels, Belgium. ✉e-mail: monika.aidelsburger@physik.uni-muenchen.de

Supplementary Information: Realization of an anomalous Floquet topological system with ultracold atoms

Karen Wintersperger[1,2], Christoph Braun[1,2,3], F. Nur Ünal[4,5], André Eckardt[4,6], Marco Di Liberto[7], Nathan Goldman[7], Immanuel Bloch[1,2,3], Monika Aidelsburger[1,2]

[1] *Fakultät für Physik, Ludwig-Maximilians-Universität München, Schellingstraße 4, 80799 München, Germany*
[2] *Munich Center for Quantum Science and Technology (MCQST), Schellingstraße 4, 80799 München, Germany*
[3] *Max-Planck-Institut für Quantenoptik, Hans-Kopfermann-Straße 1, 85748 Garching, Germany*
[4] *Max-Planck-Institut für Physik komplexer Systeme, Nöthnitzer Straße 38, 01187 Dresden, Germany*
[5] *T.C.M. Group, Cavendish Laboratory, University of Cambridge, JJ Thomson Avenue, Cambridge CB3 0HE, UK*
[6] *Institut für Theoretische Physik, Technische Universität Berlin, Hardenbergstraße 36, 10623 Berlin, Germany*
[7] *Center for Nonlinear Phenomena and Complex Systems, Université Libre de Bruxelles, CP 231, Campus Plaine, B-1050 Brussels Belgium*

Here, we present calibration measurements and additional data (S1), the detailed theoretical model (S2), the calculation of the edge states in a tight-binding model (S3) and the connection between the topological charge and the Berry curvature (S4).

S1. CALIBRATIONS AND ADDITIONAL MEASUREMENTS

A. Influence of the harmonic trap

We apply a force on the cloud by accelerating the lattice, which leads to a longitudinal velocity of the atoms in the lab frame. Detuning the frequency of one laser beam by $\Delta f = \Delta\omega/(2\pi)$ changes the quasimomentum of the atoms by

$$\Delta q = \frac{2\lambda_L m_\mathrm{K} \Delta f}{3\hbar}. \tag{S.1}$$

Changing the laser frequency linearly for a time Δt gives rise to the force:

$$F = \frac{\hbar \Delta q}{\Delta t} = m_\mathrm{K} a_L. \tag{S.2}$$

The force is varied by changing the time Δt and keeping the final detuning fixed. For the bandgap measurements the applied forces are large and Δt is small, leading only to minor displacements in real space, so in this case the effect of the harmonic trap can be neglected. The transverse deflections were probed with smaller forces to ensure that we adiabatically move within a single band, yielding real-space displacements up to $\approx 100\,\mu$m. In the presence of the harmonic trap the semiclassical equations of motion read:

$$\begin{aligned}
\dot{x} &= \frac{1}{\hbar}\frac{\partial \varepsilon}{\partial q_x}(\mathbf{q}) - \frac{1}{\hbar}\left(F_y - \frac{\partial V_\mathrm{trap}}{\partial y}\right)\Omega(\mathbf{q}) + \frac{F_x}{m_\mathrm{K}}t \\
\dot{y} &= \frac{1}{\hbar}\frac{\partial \varepsilon}{\partial q_y}(\mathbf{q}) + \frac{1}{\hbar}\left(F_x - \frac{\partial V_\mathrm{trap}}{\partial x}\right)\Omega(\mathbf{q}) + \frac{F_y}{m_\mathrm{K}}t \\
\dot{q}_x &= \frac{1}{\hbar}\left(F_x - \frac{\partial V_\mathrm{trap}}{\partial x}\right) \\
\dot{q}_y &= \frac{1}{\hbar}\left(F_y - \frac{\partial V_\mathrm{trap}}{\partial y}\right),
\end{aligned} \tag{S.3}$$

where the trapping potential is given by $V_\mathrm{trap} = 0.5 m_\mathrm{K}\omega_r^2(x^2+y^2)$ with the mean trapping frequency in the xy-plane being $\omega_r = 2\pi \times 27.0(4)\,$Hz (see below). The additional acceleration terms arise due to the motion of the lattice potential when transforming back into the lab frame and give rise to the longitudinal displacements mentioned above. In these cases the restoring force of the harmonic trap becomes significant along the direction of the force leading to a reduction of the longitudinal displacement and quasimomentum. Hence, a different amount of Berry curvature is traversed in reciprocal space, potentially changing the transverse deflection. In Fig. S1a, the calculated longitudinal quasimomenta are shown for different forces applied along the Γ-direction as a function of the quasimomentum q_f set by the lattice acceleration according to Eq. (S.1). At $q_x = q_0 = 0.5\sqrt{3}\,k_L$, the changes are minor, even for the smallest force of $Fa/h = 170\,$Hz that was used for the parameter scan in Fig. 3 in the main text. But at the final value of $q_f = 1.5\sqrt{3}\,k_L$ the quasimomentum is reduced to $q_\mathrm{eff} \approx 1.25\sqrt{3}\,k_L$.

Along the transverse direction the real space displacements are small leading only to minor changes in the quasimomentum due to the trap. To calculate the transverse deflections we numerically solved the set of equations in (S.3) including the band dispersion and the harmonic trap. The resulting transverse quasimomentum components were $q_\perp \leq 0.005\,k_L$ for all modulation parameters used in this work, meaning that the transverse band derivative is negligible, since the paths in reciprocal space are still well directed along the high-symmetry

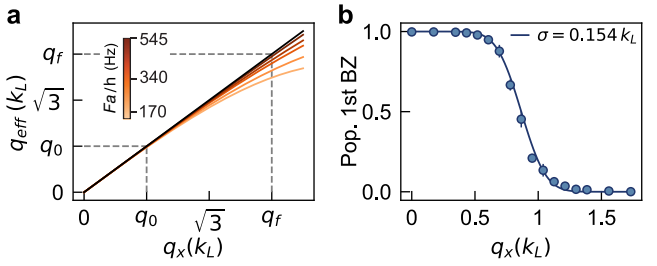

Figure S1. Calculated longitudinal quasimomentum center of mass (CoM) and calibration of the momentum space width. **a**. Calculated quasimomentum CoM q_{eff} along the direction of the force as a function of the programmed quasimomentum q_x in the presence of the harmonic trap and a static lattice with $V = 6\,E_r$ (see Sec. S2). The force is applied along the Γ-direction and varied between $Fa/h = 170\,\text{Hz}$ and $Fa/h = 545\,\text{Hz}$, as indicated by the colorbar, and $\sigma = 0.139\,k_L$. The black line is the solution without the harmonic trap. The dashed lines mark the quasimomentum $q_0 = 0.5\sqrt{3}\,k_L$ up to which we accelerate during the parameter ramp-up in many cases, and the final quasimomentum $q_f = 1.5\sqrt{3}\,k_L$. **b**. Measurement of the momentum space width by observing the population transfer when driving adiabatically across the border of the first BZ. Each point is an average over five individual experimental realizations, errorbars indicate the standard error. The solid line is an errorfunction fitted to the data to determine the Gaussian width σ.

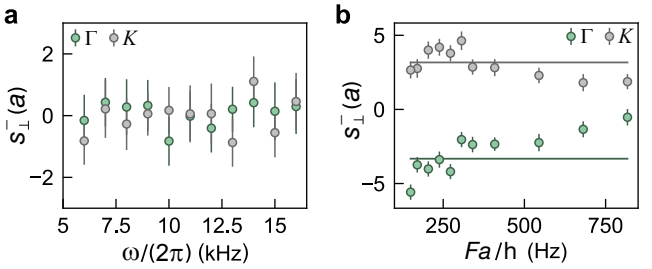

Figure S2. Transverse deflections $s_\perp^-$ in the Haldane and anomalous regime. **a**. Deflections vs. modulation frequency up to q_0 along the Γ- and K-directions with $Fa/h = 204\,\text{Hz}$ for $m = 0.25$. Errorbars indicate the SEM. **b**. Deflections in the anomalous regime ($m = 0.24, \omega/(2\pi) = 10\,\text{kHz}$) for $q_0 \to q_{\text{eff}} \approx 1.25\sqrt{3}\,k_L$ depending on the applied force. The solid lines denote the corresponding theoretical values including the momentum space width. Errorbars indicate the SEM.

lines of the lattice. Hence, it is justified that that the transverse deflection measured in the experiments is indeed proportional to the Berry curvature.

The trapping frequency was measured in the presence of a static lattice with $V = 6\,E_r$ by observing the breathing mode of the BEC insitu after a quench of the in-plane harmonic confinement. We fitted a 2D Gaussian to the absorption images, with the principle axes directed along the propagation directions of the trapping beams in the xy-plane, to extract the oscillation of the real-space width. In our system, the trapping frequency along the vertical direction is about 8-times larger than the in-plane frequency. According to [1], the in-plane trapping frequency can thus be extracted from the frequency f_b of the breathing mode as:

$$f = \sqrt{\frac{3}{10}} f_b.$$

The corresponding trapping frequencies along the dipole axes were $f_X = 27.9(7)\,\text{Hz}$ and $f_Y = 26.8(4)\,\text{Hz}$ giving the weighted average value of $f = 27.0(4)\,\text{Hz}$ mentioned above.

B. Momentum space width

Due to finite temperatures, harmonic confinement and on-site interactions, the BEC is broadened in reciprocal space, which we describe by a symmetric Gaussian momentum distribution with width σ. The width was determined experimentally by performing a knife-edge measurement in reciprocal space: The quasimomentum is changed adiabatically by one reciprocal lattice vector along the Γ-direction using a force of $Fa/h = 204\,\text{Hz}$ and performing bandmapping [2] at certain quasimomenta along the path. Since the velocity component imposed by the moving lattice is directed opposite to the Bloch oscillation, the atoms appear, when bandmapping, at the Γ-point within the first BZ. When some of the atoms reach the edge of the BZ they appear at the Γ-point in the next BZ, so we count the relative population in the first BZ (similar to the bandgap measurements) depending on the quasimomentum. The amount of atoms in the first BZ is given by the integral over the Gaussian distribution and hence described by an errorfunction. An exemplary measurement is depicted in Fig. S1b along with the resulting fit. The width of the error function was obtained from the fit, all other parameters were fixed. For every measurement of the transverse deflections we determined the width in reciprocal space immediately before or after the measurement and used this to calculate the corresponding theory values (see Sec. S2 B).

C. Deflections during ramp-up and test of the used forces

To probe the Berry curvature in the Haldane and anomalous regime the modulation amplitude and partly the modulation frequency were ramped up while driving to q_0. Using the band structure calculations we verified that during the ramp-up the points where the two lowest bands potentially had touched and hybridized, which is the location of the additional negative Berry curvature in the anomalous phase, is always located away from the edge of the moving cloud in reciprocal space (see Methods). Since we are accelerating along high-symmetry lines in reciprocal space, the band derivatives along the

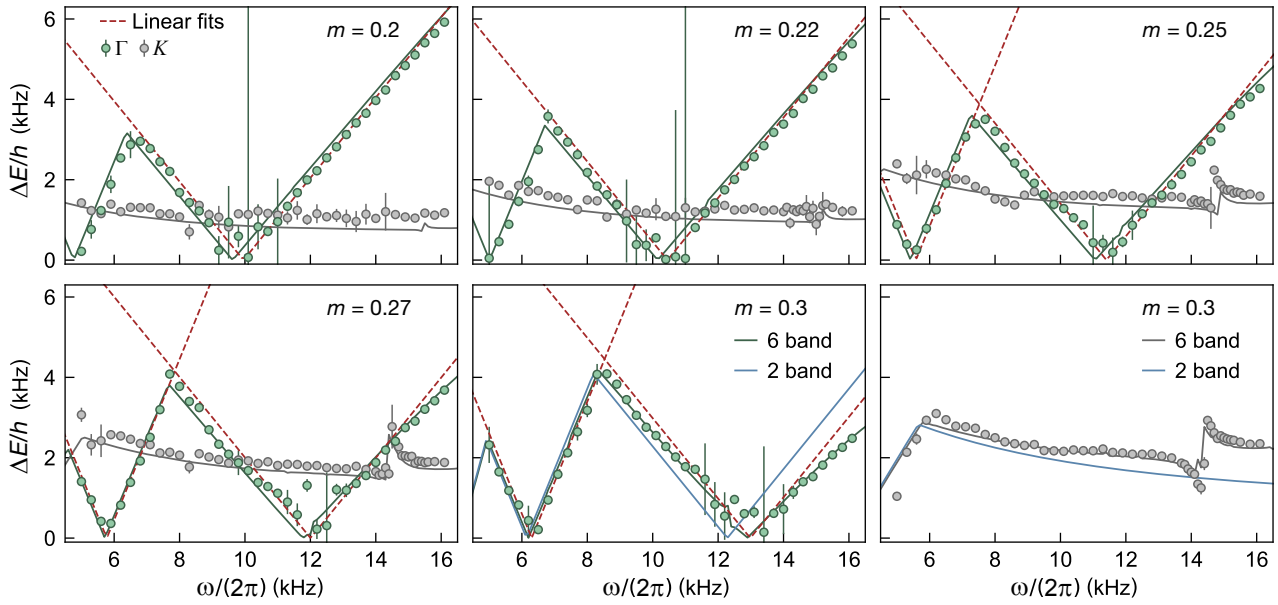

Figure S3. Energy gaps ΔE at Γ and K depending on the modulation frequency for modulation amplitudes $m = \{0.2, 0.22, 0.25, 0.27, 0.3\}$ measured with Stückelberg interferometry using $Fa/h = 1360\,\mathrm{Hz}$. The energy gap at K (gray circles) remains open over the full parameter range. The gap at Γ shows multiple closings, indicating the transitions from the Haldane to the anomalous and third phase with decreasing frequency. With increasing amplitude an avoided crossing appears at modulation frequencies around $\omega/(2\pi) = 15\,\mathrm{kHz}$. The solid green and grey lines are the corresponding theoretical minimal gaps calculated using six bands, the solid blue lines in the last two panels are the theoretical gaps from a two-band model (see Sec. S2). The red dashed lines are fits $\propto |\omega|$ to the bandgaps at Γ to determine the phase transitions (see text). The errorbars indicate fitting errors from the oscillation fits, every oscillation consists of 23 points each averaged over 3-4 individual experimental realizations.

transverse direction average to zero. Hence, there should be no deflection during the ramp-up and the measured transverse deflection can be assumed to correspond to a path in reciprocal space starting at q_0. This is confirmed by the data in Fig. S2a, showing the measured transverse deflections along the Γ- and K-direction up to a distance of q_0 for $m = 0.25$ and different modulation frequencies.

We also verified that the forces we used to measure the transverse deflections were sufficiently small to avoid a reduction of the deflections due to excitations to the second band. We measured the deflections depending on the applied force when driving by $q_{\mathrm{eff}} \approx 1.25\sqrt{3}\,k_L$ along the Γ- and K-directions for modulation parameters in the anomalous regime (see Fig. S2b). The final quasimomenta for the lattice acceleration were chosen such that the effective length of the traversed path in reciprocal space was similar for all forces. For $Fa/h > 300\,\mathrm{Hz}$, the deflections along both directions are smaller than predicted by the theoretical calculations due to excitations to the second band. The modulation parameters chosen here lie close to the phase transition with energy gaps $\Delta E(K)/h = 1500(30)\,\mathrm{Hz}$ and $\Delta E(\Gamma)/h = 1110(70)\,\mathrm{Hz}$. The measured deflections saturate for smaller forces which happens earlier along the K-direction, also indicating the larger energy gap compared to Γ. In total, the chosen forces of $Fa/h = 170\,\mathrm{Hz}$ and $Fa/h = 204\,\mathrm{Hz}$ used for these modulation parameters are sufficiently small, which is also confirmed by the overall good agreement between the measured deflections and the theoretical calculations, where we assume population in a single band.

D. Bandgap measurements for frequency scans

To explore the phase diagram shown in Fig. 1c we probed the bandgaps and Berry curvature for a broad range of modulation parameters in different topological regimes. The measured transverse deflections along the Γ- and K-directions are shown in the main text in Fig. 4a accompanied by the experimentally determined phase transitions. The corresponding gap measurements at Γ and K are displayed in Fig. S3 together with the theoretical values from our model including the six lowest energy bands. For $m = 0.3$ we also show the result of a model truncated to the lowest two energy bands. At the phase transitions, the (absolute) energy gap at Γ closes and reopens linearly with the modulation frequency for constant modulation amplitude. To determine the phase transition points, we fitted $\Delta E/h = n \cdot |\omega - \omega_0|/(2\pi)$ to the slope on the left and right of the gap closings, with $n = 1$ and $n = 2$ for the first and second phase transition. The second phase transition could only be obtained for $m \geq 0.25$. The errors for the phase transitions are $\sigma_{\mathrm{tot}} = \sqrt{\sigma_{\mathrm{fit}}^2 + \sigma_{\mathrm{sys}}^2}$ with the fit errors σ_{fit} and the sys-

tematic errors σ_{sys}. The latter are given by the step size $\Delta\omega/(2\pi) = 300\,\mathrm{Hz}$ used in the energy gap measurements which is dominating the fit errors $\sigma_{\mathrm{fit}} \in [20, 70]\,\mathrm{Hz}$.

We also measured the energy gaps at K to validate our theoretical calculations and pick the forces for the deflection measurements appropriately. For large modulation frequencies and amplitudes the influence of the p-bands becomes significant which can be seen in the jumps of the energy gap around $\omega/(2\pi) = 15\,\mathrm{kHz}$: Due to the coupling between the different bands, gaps open at avoided crossings, which increase with modulation amplitude. These manifest in discontinuities in the effective Floquet bands and the corresponding energy gaps. The experimental data is well reproduced by a six-band model, signaling that coupling to even higher bands with $\mu > 6$ can be neglected. A two-band model fails to capture all signatures of the experimental data, as illustrated by the comparison for $m = 0.3$ in Fig. S3: The overall shape of the energy gap at Γ is similar, but the first phase transition is shifted, whereas the difference between the two models decreases for smaller modulation frequencies. This is expected since the modulation frequency becomes more detuned from the energy gap to the p-bands. At K, the theoretical curves also coincide at small frequencies but in the Haldane regime the deviations are larger, especially the jumps at the avoided crossings are not captured by a two-band model. The general mechanism of the phase transitions is captured by a simple two-band model but to quantitatively describe the experiments performed here, a six-band model is necessary.

E. Stückelberg interferometry

All energy gaps presented in this work were measured using Stückelberg interferometry as described in the Methods. To quantify the amount of atoms in the first and second band, we take absorption images after performing bandmapping at Γ giving distinct peaks corresponding to the different bands, as shown in the insets of Fig. S4a. The atoms in the lowest band appear in the center, whereas atoms in the second to sixth band are distributed over the outer peaks. The forces were chosen sufficiently large to ensure population of the second band but not too large to avoid excitations to the p-bands which can also be assumed to be small due to the good agreement of the measured energy gaps with the calculated minimal gaps. We sum up the pixels inside each of the seven regions of interest (ROIs) drawn as yellow circles with radius R in the insets of Fig. S4a. To account for inhomogeneities in the background due to the finite size of the imaging beam, we also count the pixels in a larger ROI with radius $\sqrt{2}R$ (grey circles). The pixel counts for each peak are then obtained as $2\Sigma_R - \Sigma_{\sqrt{2}R}$ and the relative population in the lowest band is given by the counts in the central peak divided by the total counts.

An example of the population oscillations at Γ for different modulation frequencies and $m = 0.25$ is presented in Fig. S4a, already showing the decrease of the oscillation frequency towards the phase transitions. To obtain the points in Fig. 2 and Fig. S3 we fit a sum of cosines to each population curve as described in the Methods section of the main text. However, the change in the oscillation frequency can also be seen directly by performing a Fast Fourier transform (FFT) of the population oscillation (Fig. S4b) where the gap closings at the two phase transitions are clearly visible as well as additional small frequency components appearing around $\omega/(2\pi) = 10\,\mathrm{kHz}$ probably arising from weak coupling to Floquet copies of the p-bands.

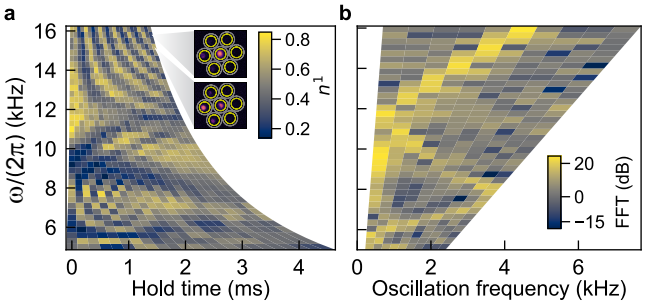

Figure S4. Raw data used to obtain the energy gaps. **a**. Relative population n^1 in the lowest band measured at Γ depending on the hold time for different modulation frequencies and $m = 0.25$. The reduction of the energy gap and thus oscillation frequency is clearly visible illustrating the gap opening and closing. Each population is an average over 3-4 individual experimental realizations. The two insets show raw images for $\omega/(2\pi) = 15.8\,\mathrm{kHz}$ and $\omega/(2\pi) = 15.2\,\mathrm{kHz}$ after a hold time of 22 modulation cycles, brighter color indicates higher optical depth. The yellow and grey circles indicate the areas used to define the pixel counts in each band and the corresponding background (see text). **b**. Fast Fourier transform (FFT) of the signal in **a** as a function of the Stückelberg oscillation frequency.

F. Lifetimes

We measured the lifetime of the BEC at Γ in all three topological regimes probed in this work. As described in the main text, in the anomalous phase the first band of the static lattice is adiabatically connected to the second band of the modulated lattice which has an energy minimum at Γ. Hence we probed the lifetime for the anomalous regime in the second band by ramping the modulation frequency and amplitude simultaneously in a nonlinear fashion (see Methods) to directly access the anomalous regime. The third regime was probed in the first band, using a similar ramp-up but starting at a smaller modulation frequency. After ramping up the modulation we held the atoms at the Γ-point in the modulated lattice for different times $t = nT$ with $n \in \mathbb{N}$, then ramped down the modulation and performed bandmapping after

10 ms TOF. In the Haldane regime (for amplitude and phase modulation) the ramp time was fixed to $5T$, in the anomalous and third regime we used $12T$ and $7T$-$8T$ respectively, corresponding to ≈ 2 ms. The population in the lowest band was then counted as $\Sigma^1 = 2\Sigma_R - \Sigma_{\sqrt{2}R}$ for the central peak using the main and background ROIs described above for the Stückelberg oscillations. The population exhibited an exponential decay as a function of the hold time for most modulation parameters, so we fitted the function $\Sigma^1(t) = Ae^{-t/\tau} + y_0$ to it and extracted the parameters A, y_0 and the lifetime τ, whereas all of them were constrained to be real and positive. The fitted offset was negligible in most cases, since we measured up to times t at which almost no atoms were left.

In the Haldane regime (Fig. S5a) we compared the lifetime for different modulation amplitudes at $\omega/(2\pi) = 10$ kHz and for $m = 0.1$ at $\omega/(2\pi) = 20$ kHz. The lifetimes increase linearly for smaller modulation amplitudes and larger frequencies moving away from the first phase transition. The value for $m = 0.1$ and $\omega/(2\pi) = 20$ kHz is comparable to the lifetime in the static lattice. In the anomalous regime (Fig. S5b) the lifetimes are much smaller and depend mainly on the modulation frequency. For $\omega/(2\pi) = 7$ kHz the system is deep in the anomalous regime and exhibits similar lifetimes for all amplitudes, whereas the lifetime is reduced significantly for $\omega/(2\pi) = 10$ kHz and slightly decreases with the modulation amplitude. In the third regime (Fig. S5c) the lifetimes increase again and strongly depend on the modulation amplitude and frequency. The parameters were chosen such that they have equal distance to the phase transition and the lifetimes are reduced by almost two orders of magnitude for larger amplitudes and higher frequencies. Based on the observed dependence of the lifetimes on the modulation parameters, we assume that these effects mainly originate from excitations to higher quasienergy bands, which are favored for larger modulation amplitudes and frequencies, increasing the coupling between the Floquet zones. In the Haldane regime, the lifetime increases for $f = 20$ kHz compared tor $f = 10$ kHz, which can be understood as follows: At $f = 20$ kHz, $g^{\pi}(\Gamma) > g^0(\Gamma)$, reducing the coupling to the first Floquet copy of the second band, whereas the gap to the corresponding p-bands is still large. Increasing the modulation frequency further, reduces the lifetime again, since excitations to the p-bands are favored: For $f = 30$ kHz and $m = 0.1$ the measured lifetime is similar as for $f = 10$ kHz (not shown in the plot).

The last panel of Fig. S5 shows the lifetimes in the Haldane regime as a function of the scattering length which we can tune using a Feshbach resonance (see main text). All measurements so far were performed at $a_s = 6.35\,a_0$. Increasing the on-site interaction considerably reduces the lifetimes in the static lattice, but even more in the modulated case, where the minimal lifetime is $\tau \approx 15$ ms for $a_s = 80.25\,a_0$. This suggests that there are also two-particle processes involved increasing the rate of excitations to higher Floquet bands.

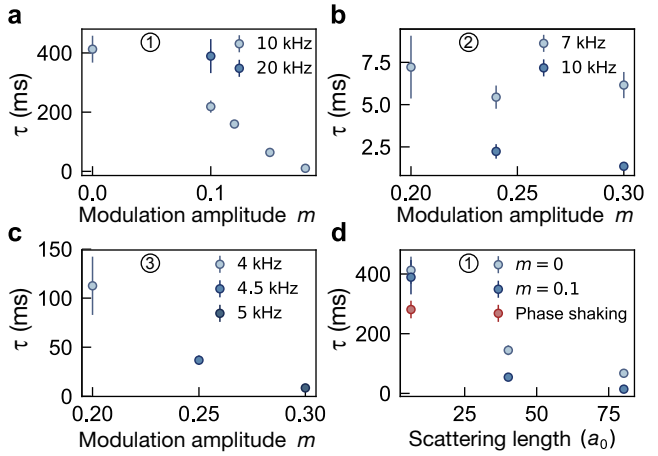

Figure S5. Measured lifetimes τ at Γ vs. modulation parameters. **a**. Haldane regime in the first band for $a_s = 6.35\,a_0$. **b**. Anomalous regime in the second band for $a_s = 6.35\,a_0$. **c**. Third regime in the first band for $a_s = 6.35\,a_0$ whereas the modulation amplitude and frequency were chosen such that the gap at Γ is similar. **d**. Haldane regime in the first band for $\omega/(2\pi) = 20$ kHz vs. scattering length. The red data point is measured for phase modulation of the lattice with a frequency of 8 kHz and an amplitude of 6.6 kHz also realizing a Haldane system with the energy gap at K calculated to be $\Delta E/h = 160$ Hz similar to the measured value for $\omega/(2\pi) = 20$ kHz and $m = 0.1$. Errorbars indicate fitting errors in all cases, every decay measurement consists of 23 points each averaged over 10 experimental realizations.

Overall, the smallest lifetimes measured are on the order of 2 ms in the second band and the anomalous regime being comparable to the maximal duration of ≈ 6 ms used in the deflection measurements. During these experiments the influence of the atom loss on the insitu images was minor, allowing for proper determination of the CoM-position by Gaussian fits in all cases. In the bandgap measurements the atom loss and heating was visible in the absorption images at long hold times, leading to damping of the oscillations.

We also compared the lifetimes in the Haldane regime to the case of a Haldane system realized by circular phase modulation of the lattice (red data point in Fig. S5d), similar to [3, 4]. Here, the lattice was shaken at a frequency of $\omega_M/(2\pi) = 8$ kHz with an amplitude $b_M/(2\pi) = 6.6$ kHz leading to an energy gap of $\Delta E/h = 160$ Hz at the K-points which is similar to the corresponding gap for $m = 0.1$ and $\omega/(2\pi) = 20$ kHz. The phase shaking leads to a reduced lifetime compared to the amplitude modulation, which is nevertheless large with respect to the experimental times used here.

S2. NUMERICAL CALCULATIONS

A. Effective Hamiltonian and energy bands

In the experiments, we directly probe the properties of the bulk from which we can deduce the topological winding numbers associated with the band gaps. These topological invariants determine the existence of chiral edge modes in the system (not measured in the experiment). To obtain the bulk energy bands and corresponding Berry curvatures in the modulated lattice we numerically calculated the effective Hamiltonian H_{eff}, which is defined via the time-evolution operator $U(T)$ over one full period of the drive:

$$H_{\text{eff}} = \frac{i\hbar}{T}\ln(U(T)), \quad U(T) = \mathcal{T}e^{-\frac{i}{\hbar}\int_0^T H(t)dt}, \tag{S.4}$$

where $\mathcal{T}$ denotes time-ordering and ln the matrix logarithm. To numerically calculate H_{eff}, the time-dependent Hamiltonian is evaluated at 300 discrete timesteps t_l within one driving period. We set $T = 1$ for the integration over one driving period to simplify the numerics. For each set of parameters $(\mathbf{q}, m)$ we calculated the instantaneous Hamiltonian $H(t_l, \mathbf{q}, m)$ at each timestep t_l in the basis of plane waves and projected it to its six lowest eigenstates:

$$H_p^*(t_l, \mathbf{q}, m) = M^\dagger(t_l, \mathbf{q}, m) \cdot H(t_l, \mathbf{q}, m) \cdot M(t_l, \mathbf{q}, m),$$

where the columns of the matrix M are the eigenstates of H corresponding to the six lowest eigenvalues and $\cdot$ denotes matrix multiplication. The resulting 6×6-matrices H_p^* are then transferred to a common basis consisting of the six lowest eigenstates of $H(t = 0, \mathbf{q} = 0, m = 0)$, being the columns of the Matrix M_0. The basis change is done as:

$$H_p(t_l, \mathbf{q}, m) = B(t_l, \mathbf{q}, m) \cdot H_p^*(t_l, \mathbf{q}, m) \cdot B^{-1}(t_l, \mathbf{q}, m),$$
$$B(t_l, \mathbf{q}, m) = M_0^\dagger \cdot M(t_l, \mathbf{q}, m).$$

The time-evolution operator is then calculated from the projected Hamiltonians at each timestep:

$$U(T, \mathbf{q}, m, f) = \Pi_l e^{-\frac{i}{\hbar}H_p(t_l, \mathbf{q}, m)\frac{\Delta t}{f}}, \tag{S.5}$$

with $f = \omega/(2\pi)$, and the effective Hamiltonian (in units of $\hbar\omega$) is given by

$$H_{\text{eff}}(\mathbf{q}, m, f) = \frac{i}{2\pi}\ln(U(T, \mathbf{q}, m, f)). \tag{S.6}$$

Due to the periodic driving, the energies are not bounded any more and the band of H_{eff} that is connected to the lowest band of the static Hamiltonian not necessarily appears as the lowest. In our case, we are interested in the two lowest bands, which are adiabatically connected to the two s-bands of the static lattice.

To extract the two lowest bands, we scanned the quasimomentum across the first BZ, calculated the six eigenstates and eigenenergies of each $H_{\text{eff}}(\mathbf{q}, m, f)$ and determined which of the states had the maximal overlap with the first and second eigenstate from the last $\mathbf{q}$-step. For the initial step we considered the overlap with the first two unit vectors, being the eigenstates of the two lowest bands in the static lattice. The state overlap is defined as the fidelity $\mathcal{F}_{ij}$:

$$\mathcal{F}_{ij} = |\langle\phi(\mathbf{q}_i, m, f)|\,|\phi(\mathbf{q}_j, m, f)\rangle|^2. \tag{S.7}$$

Especially at high modulation frequencies and amplitudes, all six bands couple and many avoided crossings appear. In the vicinity of these points, the eigenstate-overlap decreases and there can be several states having an overlap of similar magnitude with the first or second state of the last step. If the overlap with the previous eigenstate dropped below a certain threshold, we used the overlap with the unit vectors instead to avoid false attributions. The threshold value depends on the modulation parameters, i.e., for low modulation frequencies it could be set to 0.5, using the eigenstate-overlap mostly everywhere. By checking the bands in the first BZ as well as on a 1D-high-symmetry line ($\Gamma - M - K - \Gamma$), we determined the optimal limits for the fidelity for each band and set of modulation parameters. The results for two bands shown in Fig. S3 were obtained by the same procedure but projecting the instantaneous Hamiltonian at each time step to its two lowest eigenstates.

B. Transverse deflections

From the eigenstates of the two lowest bands we numerically calculate the Berry curvature according to Ref. [5] on a rhombic grid spanning the first BZ. For the numeric integration of Eq. (S.3) we interpolate the Berry curvature and the band derivatives on a large quadratic grid spanning several BZs to be able to simulate the full trajectory including the momentum space extent of the BEC. The stepsize of the quadratic grid is $dq \approx 0.0145\,k_L$ which was the maximal value at which the resulting real space positions did not change when decreasing the stepsize further.

For most modulation parameters in the experiment, we effectively probed the deflections starting at a distance of q_0 in reciprocal space after ramping up the modulation parameters. The quasimomentum after the ramp-up drive remains as $q_{||} \approx q_0$ and $q_\perp = 0$, and hence $s_\perp = 0$ (see Sec. S1 C). The longitudinal offset in real space was calculated by solving Eq. (S.3) with $\Omega(\mathbf{q}) = 0$, starting at Γ and applying the respective force along the Γ- and/or K-direction for a time Δt corresponding to q_0. The integration was performed for about 7300 initial points in quasimomentum space lying on a circle with

radius $0.5\,k_L$ around Γ to each of which we assigned a Gaussian weight according to the normalized momentum distribution of the BEC with width σ. The CoM position and quasimomentum after the ramp-up were then given as the weighted average over the corresponding final values. Note that we used the band derivatives for the final modulation parameters here, which turned out to give similar results as directly simulating the ramp-up by using the band derivatives for the different modulation parameters taken in between.

The deflections were then calculated by integrating Eq. (S.3) along the Γ- and K-direction with the initial points lying on a circle centered around the starting point after the ramp-up, given either by the values above or, when measuring along the Γ-direction in the first band and third regime or the second band and anomalous regime, by $q_{||} = 0 = q_\perp$ (see Methods). The time span was determined by the corresponding force and the programmed quasimomentum distance of $1.5\sqrt{3}\,k_L - q_0$ (or $1.0\sqrt{3}\,k_L$, respectively). The CoM deflection and quasimomentum were obtained as the average over the final values, again using the Gaussian weights of the independently calibrated density distribution. For modulation parameters lying in between the experimental points, the Gaussian width of the closest measured point was used. The approximate final values q_{eff} for the longitudinal quasimomentum mainly depend on the magnitude of the applied force and the time for which it is applied, whereas the influence of the band derivatives and the force direction is negligible.

S3. CALCULATION OF EDGE STATES IN A TIGHT-BINDING MODEL

As described in the main text, in a periodically-driven system the net number and chirality of edge modes per energy gap is given by the winding number of the respective gap, allowing for a full characterization of the system using topological invariants of the bulk only. In addition to the determination of the winding numbers we also calculated the energy spectrum of the effective Hamiltonian on a stripe-geometry displaying the dispersion of the edge states directly. We employed a two-band tight-binding model defined on a stripe terminated by an armchair-edge in the y-direction and with periodic boundary conditions along x (Fig. S6a).

Due to hybridization between the s- and p-bands for large modulation frequencies, the lowest six energy bands have to be taken into account to quantitatively understand the position of the phase transitions for the model realized in our experiment (Sect. S2 A). Considering only the two lowest bands results in a shift of the transition points (see last two panels of Fig. S3), but the general nature of the topological phase diagram remains unchanged. In this section we present an approximate description based on a two-band tight-binding model with time-dependent nearest-neighbor hoppings that allows us to compute the dispersion of the edge modes directly.

The modulation of the relative intensities leads to a modulation of the distance between neighbouring lattice sites, which can be expressed as time-dependent tunneling matrix amplitudes in the tight-binding limit. The unit cell of the stripe consists of N dimers along the y-direction and has a width of $3a$ in the x-direction. Due to the periodicity along x, the Hamiltonian can be Fourier-transformed along this direction with quasimomentum $q_x \in [-\frac{\pi}{3a}, \frac{\pi}{3a}]$. Including time-dependent nearest-neighbour tunneling along the directions $\delta_{\mathbf{i}}$ with amplitudes $J_i(t)$, $i = \{1,2,3\}$ and setting the energy offset between the A- and B-sites to zero, the Hamiltonian reads

$$\begin{aligned}\hat{H}_{\text{tb}}(q_x,t) = &-\sum_{n,q_x} J_1(t)\left(e^{-iq_x a}\hat{\alpha}^\dagger_{q_x}(n)\hat{\beta}_{q_x}(n) + c.c.\right)\\ &+ J_2(t)\left(e^{iq_x\frac{a}{2}}\hat{\alpha}^\dagger_{q_x}(n)\hat{\beta}_{q_x}(n+1) + c.c.\right)\\ &+ J_3(t)\left(e^{iq_x\frac{a}{2}}\hat{\alpha}^\dagger_{q_x}(n+1)\hat{\beta}_{q_x}(n) + c.c.\right),\end{aligned} \tag{S.8}$$

where $\hat{\alpha}^\dagger_{q_x}(n)$ and $\hat{\beta}^\dagger_{q_x}(n)$ create a particle with quasimomentum q_x on the nth A- and B-site within the stripe.

To extract the time-dependent tunneling amplitudes, we fitted the energy bands of the two-band tight-binding model for the system without boundaries to the two lowest energy bands of the full Hamiltonian for a fixed modulation amplitude at every timestep t_l within one driving period. The fit was performed on both energy bands in the entire 2D-BZ, yielding the values of $J_i(t_l)$, $i = \{1,2,3\}$ within one modulation cycle. In the full six-band Hamiltonian of our time-dependent honeycomb lattice model, particle-hole symmetry is broken resulting in an asymmetry of the two s-bands. This could be accounted for by including next-nearest-neighbour hoppings and coupling to p-orbitals, however, for a conceptual understanding of the phase diagram, the simple two-band model of Eq. (S.8) is sufficient. In general, the nearest-neighbour hopping amplitude between two sites is expected to depend exponentially on the height of the potential barrier between the sites. Hence, we described the time-dependence of the hopping amplitudes as

$$J_i(t) = A\,e^{B\cos(\omega t+\phi_i)} + C \quad i = \{1,2,3\}, \tag{S.9}$$

with $\phi_i = \frac{2\pi}{3}\times(i-1)$ and A, B and C are free variables that depend on the modulation amplitude. This function was fitted to the extracted hopping amplitudes. Using the time dependent hoppings we calculated the effective Hamiltonian by integration of $\hat{H}_{\text{tb}}(q_x,t)$ over one driving period according to Eq. (S.4) for every q_x. The resulting $2N$ quasienergies are shown in Fig. S6b as a function of the quasimomentum q_x for $N = 50$, $m = 0.25$ and different modulation frequencies describing the three topological phases. The first plot with $\omega/(2\pi) = 16\,\text{kHz}$ corresponds to the Haldane regime, where a pair of chiral edge modes is visible in the gap at zero quasienergy.

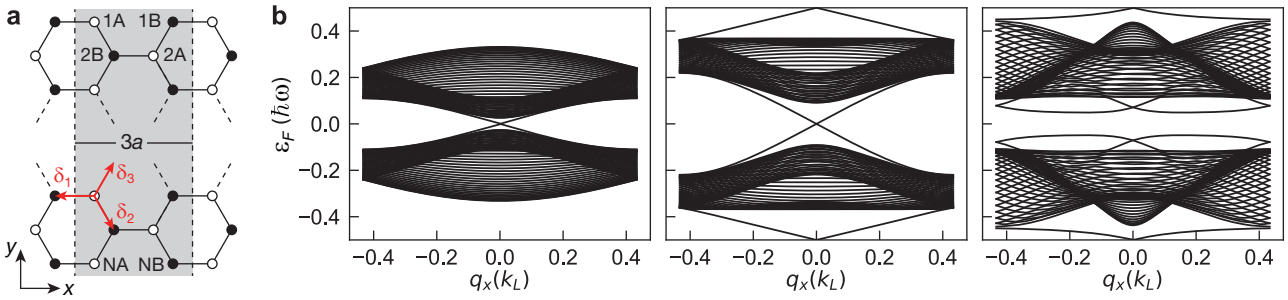

Figure S6. Schematic of the stripe-geometry and calculated quasienergy dispersions in the three topological phases plotted in the reduced zone scheme. **a**. Schematic of the stripe geometry described in the text, terminated by an armchair-edge along y and with periodic boundary conditions along x. The unit cell (gray shaded area) consists of N dimers and has a width of $3a$, the red arrows denote the vectors δ_i connecting nearest neighbours. **b**. Quasienergy dispersions from the two-band tight-binding model with $N = 50$ for a modulation amplitude of $m = 0.25$ and modulation frequencies $\omega/(2\pi) = \{16, 8, 4\}$ kHz corresponding to the Haldane regime, anomalous regime and third regime hosting chiral edge modes in the g^0-gap, both gaps and the g^π-gap, respectively.

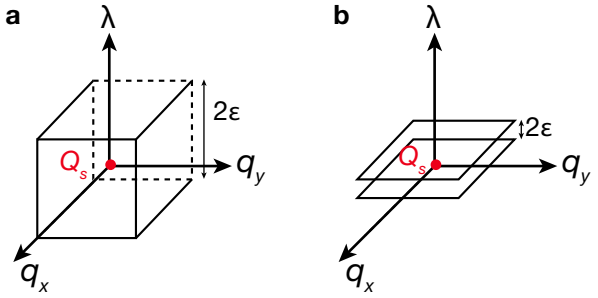

Figure S7. Schematic drawing of the topological charge Q_s and the integration surfaces discussed below. **a**. Cube with height 2ε around Q_s in the three-dimensional parameter space $(\mathbf{q}, \lambda)$. **b**. Two two-dimensional surfaces in $\mathbf{q}$-space separated by 2ε.

For a system with an armchair edge being periodic along x, the Γ- and K-point are both displayed at $q_x = 0$. At $\omega/(2\pi) = 8$ kHz the system is in the anomalous phase exhibiting an additional pair of edge modes in the g^π-gap between FBZs. In the third regime with $\omega/(2\pi) = 4$ kHz the are no edge modes at zero quasienergy in the g^0-gap, but there exist chiral edge modes in the π-gap, characterizing a Haldane-like topological system.

S4. WINDING NUMBERS AND TOPOLOGICAL CHARGE

The change in winding number across a topological phase transition is defined via the topological charge Q_s^j of the band touching singularity as defined in Eq. (1) in the main text. We consider a three-dimensional parameter space spanned by the quasimomentum $\mathbf{q}$ and λ, which smoothly connects a family of Hamiltonians $H(\mathbf{q}, \lambda)$ (white arrows in Fig. 2a). For two-band models this Hamiltonian can be expressed as $H(\mathbf{q}, \lambda) = \sum_{\alpha=x,y,z} h_\alpha(\mathbf{k})\sigma_\alpha + h_0(\mathbf{k})\mathbb{1}$, where $\boldsymbol{\sigma} = (\sigma_x, \sigma_y, \sigma_z)$ is the vector of Pauli matrices and $\mathbb{1}$ is the identity matrix. In generic cases we can make a Taylor expansion of the dispersion relation in the vicinity of the gap closing point [6] that occurs at $\xi := (\mathbf{q}_s, \lambda_s)$. The resulting Hamiltonian can be expressed in the form of a Weyl Hamiltonian

$$H_s = v_{\beta\alpha}\xi_\beta\sigma_\alpha, \tag{S.10}$$

where v is a 3×3 matrix. The topological charge of the singularity is then given by [7, 8]

$$Q_s = \mathrm{sgn}(\det(v)). \tag{S.11}$$

The Hamiltonian (S.10) has the form of a general three-parameter Hamiltonian $H_s = \mathbf{v}' \cdot \boldsymbol{\sigma}$, whose Berry curvature of the upper and lower state is described by magnetic monopoles $\boldsymbol{\Omega}^\pm = \mp\frac{1}{2}\frac{\mathbf{v}'}{v'^2}$ and there is a singularity at $\mathbf{v}'_s = 0$. The Berry flux through a closed surface Σ_c containing the singularity $\mathbf{v}'_s = 0$ is given by

$$\phi^\pm = \mp\frac{1}{2}\int_{\Sigma_c} \mathrm{d}\boldsymbol{\Sigma} \cdot \boldsymbol{\Omega}_\pm = \mp 2\pi Q_s. \tag{S.12}$$

Note that here we defined the topological charge Q_s by the Berry flux of the energy band below the respective energy gap. In Floquet systems there are two independent gaps and the topological charge Q_s^0 in the gap g^0 is defined via the Berry curvature of the lower band Ω^- and accordingly, the topological charge Q_s^π in the gap g^π is defined via the Berry curvature of the upper band Ω^+.

One possibility to measure the topological charge associated with the singularity is to determine the flux through a sphere containing the band touching point or equivalently through a cube as depicted in Fig. S7a, which would require Berry flux measurements through the six surfaces of the cube in $(\mathbf{q}, \lambda)$-space. This idea, however, can be simplified, if we consider the limit of $2\varepsilon \to 0$ and shift the origin trivially, such that the singularity located at ξ is at the origin $\xi = 0$. In this limit,

the Berry flux through the two surfaces just before and just after the phase transition (Fig. S7b) in $\mathbf{q}$-space is determined by

$$\phi^-_{\pm\varepsilon} = \int_{-q_x^0}^{q_x^0} \mathrm{d}q_x \int_{-q_y^0}^{q_y^0} \mathrm{d}q_y \quad \Omega^-_{\lambda_s \pm\varepsilon}(\mathbf{q_s})$$
$$\phi^-_{\pm\varepsilon} \quad \xrightarrow{\varepsilon\to 0} \quad \pm\pi \tag{S.13}$$

Infinitesimally away from the band-touching singularity, the Berry curvature is perfectly localized in the $q_x q_y$-plane giving rise to a flux of $\pm\pi$. Thus, in order to determine the sign of the topological charge we simply need to detect the sign of the π Berry flux on both sides of the phase transition:

$$\frac{1}{2\pi}\Delta\phi^-(\mathbf{q}_s) \quad \xrightarrow{\varepsilon\to 0} \quad Q_s^0, \tag{S.14}$$

with $\Delta\phi^-(\mathbf{q}_s) = \left(\phi^-_{+\varepsilon} - \phi^-_{-\varepsilon}\right)$. The Berry flux ϕ is proportional to our measured deflections $s_\perp$, however, in the experiment we perform a weighted average according to the momentum distribution of our condensate as discussed in Section S2 B. Nonetheless, if the spread is not too large and if we can perform the measurement close enough at the phase transition point, we can identify the topological charge of the singularity by determining the sign of the local Hall drifts across the phase transition [4, 9]:

$$Q_s^0 = \mathrm{sgn}\left(\Delta s^-_\perp(\mathbf{q}_s)\right) = -\mathrm{sgn}\left(\Delta s^+_\perp(\mathbf{q}_s)\right) \tag{S.15}$$

Equivalently, the topological charge of the π-gap is determined by

$$Q_s^\pi = -\mathrm{sgn}\left(\Delta s^-_\perp(\mathbf{q}_s)\right) = \mathrm{sgn}\left(\Delta s^+_\perp(\mathbf{q}_s)\right). \tag{S.16}$$

[1] S. Stringari, "Collective Excitations of a Trapped Bose-Condensed Gas," Phys. Rev. Lett. **77**, 2360–2363 (1996).

[2] M. Greiner, I. Bloch, O. Mandel, T. W. Hänsch, and T. Esslinger, "Exploring Phase Coherence in a 2D Lattice of Bose-Einstein Condensates," Phys. Rev. Lett. **87**, 160405 (2001).

[3] M. C. Rechtsman, J. M. Zeuner, Y. Plotnik, Y. Lumer, D. Podolsky, F. Dreisow, S. Nolte, M. Segev, and A. Szameit, "Photonic Floquet topological insulators," Nature **496**, 196–200 (2013).

[4] G. Jotzu, M. Messer, R. Desbuquois, M. Lebrat, T. Uehlinger, D. Greif, and T. Esslinger, "Experimental realization of the topological Haldane model with ultracold fermions," Nature **515**, 237–240 (2014).

[5] T. Fukui, Y. Hatsugai, and H. Suzuki, "Chern Numbers in Discretized Brillouin Zone: Efficient Method of Computing (Spin) Hall Conductances," J. Phys. Soc. Jpn. **74**, 1674–1677 (2005).

[6] J. Bellissard, "Change of the Chern number at band crossings," arXiv **cond-mat/9504030** (1995).

[7] S. M. Young, S. Zaheer, J. C. Y. Teo, C. L. Kane, E. J. Mele, and A. M. Rappe, "Dirac Semimetal in Three Dimensions," Phys. Rev. Lett. **108**, 140405 (2012).

[8] N. P. Armitage, E. J. Mele, and A. Vishwanath, "Weyl and Dirac semimetals in three-dimensional solids," Rev. Mod. Phys. **90**, 015001 (2018).

[9] M. Aidelsburger, M. Lohse, C. Schweizer, M. Atala, J. T. Barreiro, S. Nascimbène, N. R. Cooper, I. Bloch, and N. Goldman, "Measuring the Chern number of Hofstadter bands with ultracold bosonic atoms," Nature Phys. **11**, 162–166 (2015).